The Annual Cycle of the Axial Angular Momentum of the Atmosphere

JOSEPH EGGER

Meteorologisches Institut, Universität München, Munich, Germany

KLAUS-PETER HOINKA

Institut für Physik der Atmosphäre, DLR, Oberpfaffenhofen, Germany

(Manuscript received 17 December 2003, in final form 23 July 2004)

ABSTRACT

Earlier analyses of the annual cycle of the axial angular momentum (AAM) are extended to include mass flows and vertical transports as observed, and to establish angular momentum budgets for various control volumes, using the European Centre for Medium-Range Forecasts (ECMWF) Re-Analyses (ERA) for the years 1979–92, transformed to height coordinates. In particular, the role of the torques is examined. The annual cycle of the zonally averaged angular momentum is large in the latitude belt $20° \leqslant |\varphi| \leqslant 45°$, with little attenuation in the vertical up to a height of ~12 km. The oscillation of the mass term (AAM due to the earth's rotation) dominates in the lower troposphere, but that of the wind term (relative AAM) is more important elsewhere. The cycle of the friction torque as related to the trade winds prevails in the Tropics. Mountain torque and friction torque are equally important in the extratropical latitudes of the Northern Hemisphere.

The annual and the semiannual cycle of the global angular momentum are in good balance with the global mountain and friction torques. The addition of the global gravity wave torque destroys this agreement. The transports must be adjusted if budgets of domains of less than global extent are to be considered. Both a streamfunction, representing the nondivergent part of the fluxes, and a flux potential, describing the divergences/convergences, are determined. The streamfunction pattern mainly reflects the seasonal shift of the Hadley cell. The flux potential links the annual oscillations of the angular momentum with the torques. It is concluded that the interaction of the torques with the angular momentum is restricted to the lower troposphere, in particular, in the Tropics. The range of influence is deeper in the Northern Hemisphere than in the Southern Hemisphere, presumably because of the mountains. The angular momentum cycle in the upper troposphere and stratosphere is not affected by the torques and reflects interhemispheric flux patterns. Budgets for the polar as well as for the midlatitude domains show that fluxes in the stratosphere are important.

1. Introduction

The atmosphere's zonal mean axial angular momentum $\overline{\mu}$ exhibits a pronounced annual cycle [e.g., Peixoto and Oort 1992, hereafter PO; see Eqs. (1.2) and (1.3) for definitions]. For example, the midlatitude westerlies are stronger in the winter than in the summer hemisphere. The global angular momentum M oscillates during the course of the year with an amplitude of 1.9 $\times 10^7$ Hadleys (1 Hadley = 10^{18} kg m^2 s with a maximum in boreal winter (see section 3b; Oort 1989; Kang and Lau 1994; Hide et al. 1997). This seasonal variation of M accounts for more than 90% of its total variance (Rosen et al. 1991; Huang and Sardeshmukh 2000). Given the torques, the transports, and the annual cycle of the angular momentum, an attempt can be made to establish a corresponding budget of the annual cycle. Hantel and Hacker (1978), Oort and Peixoto (1983), PO, and others tackled this problem by calculating mean transports for the seasons, assuming that the tendency of the angular momentum could be neglected and that the vertical transports could be evaluated as residuals. They found, inter alia, that an intensification of the poleward relative angular momentum transports in the respective winter season and an asymmetry of the hemispheres in that the Hadley cell transports are stronger in the boreal than in the austral winter (Fig. 11.9 of PO). The eventual effect of interhemispheric cross-equatorial mass shifts on the angular momentum budget has not been considered so far, because the budgets had been derived for an atmospheric layer between the 1000-hPa surface and a constant pressure surface on top. Moreover, the annual tendency of the angular momentum has been neglected. The divergent part of the angular momentum fluxes has not been evaluated as

Corresponding author address: Joseph Egger, Meteorologisches Institut, Universität München, Theresienstr. 37, 80333 München, Germany.
E-mail: j.egger@lrz.uni-muenchen.de

yet. These omissions and approximations are partly imposed by the data used by PO and earlier authors. It is only in recent years that globally consistent datasets became available, which allow one to calculate vertical transports directly as well as the mass term. This calls for a reanalysis of the annual cycle of angular momentum and to an extension of the range of questions dealt with so far in the literature. In particular, the role of the mass term and its transports in the seasonal angular momentum budgets needs further clarification. The annual interaction of the angular momentum with torques and transports in specific regions is not known and will be investigated. In particular, we wish to determine the divergent part of the angular momentum flux so as to establish a complete budget of angular momentum.

The following analysis will be based on the zonally averaged angular momentum equation

$$\frac{\partial}{\partial t}\overline{\mu} + \frac{1}{a}\frac{\partial}{\partial \varphi}\overline{F}_h + \frac{\partial}{\partial z}\overline{F}_v = -\sum(\Delta p)\, a\cos\varphi, \qquad (1.1)$$

where the bar stands for the zonal integration

$$\overline{s} = \int_0^{2\pi} sa\cos\varphi d\lambda \qquad (1.2)$$

(a is the earth's radius, φ latitude, and λ longitude). In (1.1)

$$\mu = \rho(u + \Omega a\cos\varphi)a\cos\varphi \qquad (1.3)$$

(ρ is density, u zonal velocity, and $\Omega = 2\pi\ \mathrm{day}^{-1}$) is the angular momentum per unit volume, and

$$F_h = v\mu, \qquad (1.4)$$

$$F_v = w\mu - a\cos\varphi\tau_z + \Omega a 2\cos 2\varphi H \qquad (1.5)$$

are the related horizontal and vertical fluxes with meridional (vertical) velocity v (w), respectively. A separation of vertical fluxes $w\mu$ as resolved by an analysis scheme from a turbulent unresolved part is introduced in (1.5) where τ_z is the vertical component of the stress and H is the unresolved vertical density flux. In principle, a similar separation should be made in (1.4), but this refinement is omitted here because it is presumably unimportant. The sum on the right of (1.1) runs over all east–west pressure differences across mountain massifs intersected by the line z = constant, φ = constant for which the integration (1.2) is performed. We introduce the usual separation

$$\mu = \mu_w + \mu_m \qquad (1.6)$$

of the angular momentum in a wind term, which represents the contribution of the zonal momentum ρu to μ [first term in (1.3)], and a mass term that captures the contribution by the earth's rotation. The mass term is normally neglected partly because its seasonal variation is smaller than that of the wind term (e.g., Huang and Sardeshmukh 2000). Here, μ_m will be included.

It is convenient to introduce a Fourier decomposition

$$s = s_c\cos\omega_a t + s_s\sin\omega_a t, \qquad (1.7)$$

where $\omega_a = 2\pi\ \mathrm{yr}^{-1}$ is the annual frequency, and where the Fourier components s_c, s_s do not depend on time. Using complex notation, we write

$$\overline{s} = \mathrm{Re}[\hat{s}\exp(i\omega_a t)], \qquad (1.8)$$

where

$$\hat{s} = s_c - is_s. \qquad (1.9)$$

With that, (1.1) becomes

$$i\omega_a\hat{\mu} + \frac{1}{a}\frac{\partial}{\partial\varphi}\hat{F}_h + \frac{\partial}{\partial z}\hat{F}_v = -\sum(\Delta\hat{p})a\cos\varphi. \qquad (1.10)$$

The vertical integration of (1.10) from the topographic height h to infinity gives

$$i\omega_a\int_h^\infty \hat{\mu}dz + \int_h^\infty \frac{1}{a}\frac{\partial}{\partial\varphi}\hat{F}_h dz - (\hat{w}\mu)_{z=h} = \hat{T}_o + \hat{T}_f + \hat{T}_g, \qquad (1.11)$$

where $\hat{T}_o(\hat{T}_f)$ represents the annual component of the mountain (friction) torque per unit latitude width. The gravity wave torque $\hat{T}_g$ is included in (1.11), that is, the mountain torque due to unresolved orographic effects. As is well known, $\hat{T}_f$ contains the unresolved part of (1.5) at the lower boundary. Of course, $\hat{w} = 0$ at the surface if there is no topography. The torques on the right-hand side of (1.11) balance the annual tendency of the angular momentum and the divergence of the flux.

Integration of (1.11) over all latitudes gives the global relation

$$i\omega_a\hat{M} = \hat{T}, \qquad (1.12)$$

where $\hat{M} = \int_v\hat{\mu}dV$ represents the annual cycle of the global angular momentum, and $\hat{T}$ is the corresponding global torque.

In what follows, the Fourier components $\hat{\mu}$, etc., will be evaluated using data. In particular, the fluxes $\hat{F}_h$ and $\hat{F}_v$ are computed on the basis of the available winds and densities. This allows us to analyze (1.10). The semiannual cycle will be considered, but only briefly where ω_a in (1.7) has to be replaced by $2\omega_a$. Otherwise, the same formalism can be used as for the annual cycle.

An interesting, and rather different, approach has been chosen by Huang and Sardeshmukh (2000) who noted that the seasonal cycle of the global integral of $u\cos\varphi$ at an upper-tropospheric level serves as an excellent proxy for that of the global wind term. In turn, the vorticity equation, when adapted to this level, can be used to study the dynamics of this proxy. Huang and Sardeshmukh (2000) specified the divergence term in the vorticity equation as well as the transient-eddy terms as a forcing on the basis of data and were able to reproduce the annual cycle of the proxy fairly well. It remains to establish the link between the torques and this upper-level forcing in view of (1.12).

2. The data

The data that are to be used have been generated in the European Centre for Medium-Range Weather Forecasts (ECMWF) Re-Analysis (ERA) project (e.g., Gibson et al. 1997). They cover the years 1979–92. The winds, temperature, and density are available at the 31 levels of the hybrid σ system of the ERA scheme. Surface pressure, stress, and gravity wave drag are part of the dataset, so that all torques can be calculated. Although it would have been preferable to use the data in this original coordinate system, the height of the σ surfaces performs an annual cycle. The effect of this oscillation on the angular momentum budget is difficult to estimate. It has, therefore, been decided to transform the data to a z-coordinate system with $J = 28$ equally spaced coordinate surfaces of distance $D_z = 1000$ m. The coordinate surface z_j is located at the height

$$z_j = z_1 + (j - 1)D_z \tag{2.1}$$

($j = 1, \ldots, J + 1$), where $z_1 = 100$ m is the height of the lowest surface [see Egger and Hoinka (2004) with respect to the choice of z_1]. The center of a layer is at height $\hat{z}_j = z_j + 1/2\ D_z$. The choice of the z-coordinate system implies, of course, that μ is small in the stratosphere. The layers of the ERA system above sea level are shown in Fig. 1a, as well as those of the z-coordinate system. It is obvious from Fig. 1 that the vertical resolution of the ERA set becomes inadequate above, say, a height of 20 km, while it is quite good in the lower troposphere. In turn, details of vertical structures found above layer 21, say, are unreliable. Latitude belts of width aD_φ are defined, which are centered at the latitude

$$\hat{\varphi}_i = \varphi_{i-1} + \frac{1}{2} D_\varphi = -\frac{\pi}{2} + \left(i - \frac{1}{2}\right) D_\varphi, \tag{2.2}$$

with $1 \leqslant i \leqslant \mathrm{I}$, where $\mathrm{I} = 20$ is the total number of the belts, and $\mathrm{D}_\varphi = \pi/\mathrm{I} = 9°$. The latitude $\varphi_i = -\pi/2 + iD_\varphi$ defines the northern boundary of belt i (see Fig. 1b). Belts 1–3 (90°–63°S) and 18–20 (63°–90°N) constitute the polar regions, belts 4–7 (63°–27°S) and 14–17 (27°–63°N) represent the midlatitudes, and the Tropics are covered by belts 8–13 (27°S–27°N). These belts provide a coarse, but, as will be shown, sufficient, meridional resolution for the phenomena we want to investigate. On the other hand, the mass contained in a belt varies $\sim \cos\varphi$ with latitude. As emphasized by a referee, it might be preferable to use belts of uneven widths but equal mass contents; that is, the width of the belts must vary $\sim|\sin\varphi|$ with latitude. If that is done and if the

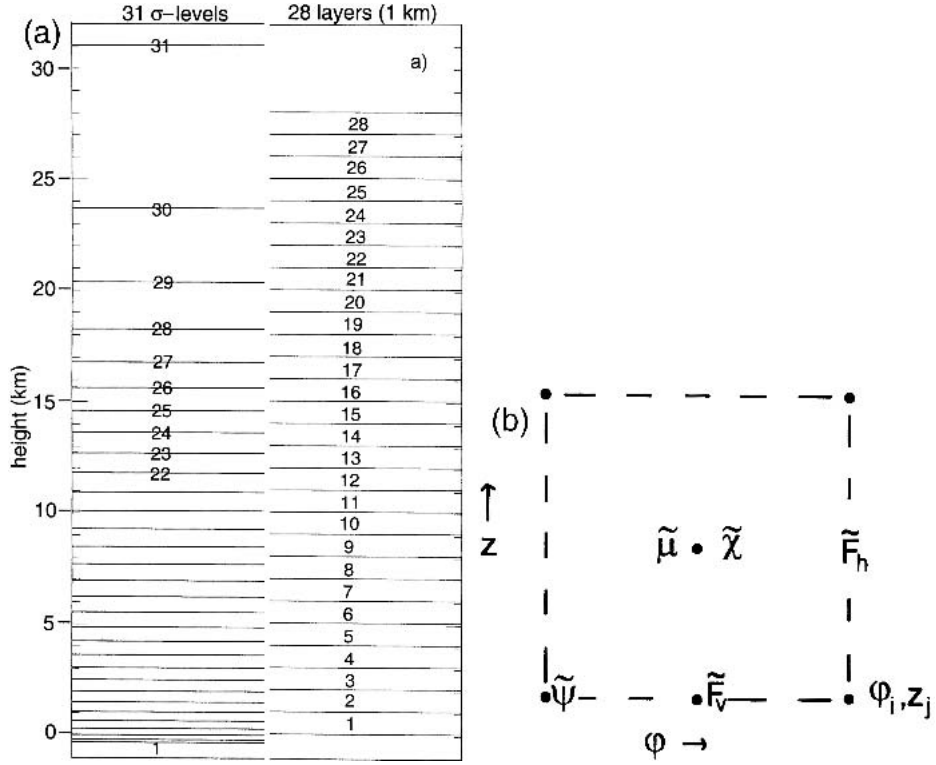

FIG. 1. (a) Mean height of the 31 coordinate surfaces of the (left) ERA system and the (right) height of the z-coordinate surfaces used in this analysis. The numbers of the z-coordinate layers correspond with the layer index j. (b) The arrangement of the variables in the analysis grid; the streamfunction ψ and the flux potential χ are defined in section 3b (see text for further details).

number of belts is kept the same, equatorial belts have a width of ~6°; those at midlatitudes are close to D_φ = 9°, while belt 20 covers the polar cap at 64°–90°N. Although the actual calculations will be carried out for the belts of fixed widths, we will refer occasionally to the effect of introducing belts of an approximately equal mass. Of course, the choice (2.1) of the layers in the vertical faces the same problem.

The intersection of the z-coordinate surfaces, with the latitudes φ_i, defines 560 annuli with indices (i, j). The data are available in a latitude–longitude grid on the sigma surfaces. The transformation to the z-coordinate system is straightforward except that some grid points are inside the topography. We impose the convention that all of those points of the (λ, φ, z) grid are inside the mountains if the center height $\hat{z}_j$ of the grid box is less than the corresponding height of the ERA orography. Such orographic boxes are excluded in the integrals (1.2) over longitude. The data are interpolated such that horizontal transports are available at the gridpoints $(\varphi_i, \hat{z}_j)$, vertical transports at $(\hat{\varphi}_i, z_j)$ and the angular momenta μ_{ij} at the center point $(\hat{\varphi}_i, \hat{z}_i)$ of annulus (i, j) (see Fig. 1b). The torques are calculated at the ground and are finally available at the latitudes $\hat{\varphi}_i$.

It is difficult to estimate the reliability of the various data. It seems reasonable to attach high credibility to the angular momenta that are calculated as products of quantities that can be determined quite accurately. The transports are presumably less reliable because they involve triple products. Moreover, the vertical velocities are not based on direct observations. Surface stresses are calculated on the basis of turbulence parameterizations of limited validity above complex terrain. On the other hand, the ERA data are the result of a consistent analysis procedure so that budget equations should be satisfied reasonably well, even if, say, the torques that are used deviate somewhat from the unknown real torques.

The time resolution of the ERA data is 6 h. The computational effort is reduced by averaging all of the variables over all four values per day. Integration of (1.10) over the latitude–height cross section of an annulus above topography with area $Q = aD_zD_\varphi$ gives

$$i\omega_a\tilde{\mu}_{ij} + (\tilde{F}_h)_{ij} - (\tilde{F}_h)_{i-1j} + (\tilde{F}v)_{ij+1} - (\tilde{F}_v)_{ij} = 0, \qquad (2.3)$$

where

$$\tilde{\mu}_{ij} = \int_Q \hat{\mu} a d\varphi dz, \qquad (2.4)$$

$$(\tilde{F}v)_{ij} = \int_{\varphi i-1}^{\varphi i} \hat{F}_v|_{z=z_j} a\, d\varphi, \qquad (2.5)$$

$$(\tilde{F}_h)_{ij} = \int_{z_j}^{z_{j+1}} \hat{F}_h|_{\varphi=\varphi_i}\, dz. \qquad (2.6)$$

The treatment of the lower boundary poses a problem in that at least the lowest z-coordinate surfaces of the (λ, φ, z) grid intersect the orography of the ERA set at various points. The torques have to be distributed over several levels to take this effect into account. A corresponding discussion is found in Egger and Hoinka (2004), where globally averaged vertical angular momentum transports are presented as well as global torques. In particular, various sets of vertical resolutions of the grid are tested. It turns out that the angular momentum budgets near the ground are affected by the specific incorporation of the topography and also by the vertical resolution. However, there is little influence above the lowest two layers, that is, above a height of 2000 m. It has been decided on the basis of this work to adopt the simplest scheme where all torques are defined at the surface z_1, so that

$$\tilde{F}_{v1} = \int_{\varphi_{i-1}}^{\varphi_i} (\hat{T}_o + \hat{T}_f + \hat{T}_g)\, a d\varphi. \qquad (2.7)$$

The Fourier coefficients s_c, s_s of a variable s are evaluated by standard Gaussian minimalization, that is,

$$s_c = \sum_n s(nDt)\cos\left(\omega_a n D_t\right) \Big/ \sum_n \cos\left(\omega_a n D_t\right)^2, \qquad (2.8)$$

etc., where D_t = 1 day and n is the time index running over all of the days of the ERA set.

The resolved vertical flux F_v as derived from the ERA data does, of course, not contain the unresolved fluxes $\sim\tau_z$ and $\sim H$, which are certainly important, at least close to the ground. The only information available on the unresolved flux is that on the torques. Moreover, the tendency $\omega_a\tilde{\mu}_{ij}$ in (2.3) tends to be at least one order of magnitude smaller than the fluxes. As will be demonstrated, the divergence of the fluxes as evaluated does not balance these small tendencies with a sufficient degree of accuracy. A way out of this dilemma is to adjust the horizontal fluxes in the sense of Gaussian minimalization [see also Hantel and Hacker (1978) and PO for similar approaches to this problem]. We require that the quadratic deviations of the adjusted fluxes $(\tilde{F}^*_h)_{ij}$ from the observed fluxes are minimal under the constraint that the vertically integrated version

$$\sum_j [i\omega_a\tilde{\mu}_{ij} + (\tilde{F}^*_h)_{ij} - (\tilde{F}^*_h)_{i-1j}] - \tilde{T}_i = 0 \qquad (2.9)$$

of (2.3) with (2.7) is satisfied for each belt where $\tilde{T}_i$ is the sum of all torques in (2.7). The details of the procedure are described in the appendix. This technique works if

$$\sum_i (\tilde{T}_i) = \sum_{ij} i\omega_a\mu_{ij}, \qquad (2.10)$$

that is, if the global angular momentum balance is satisfied exactly. This constraint is imposed by subtracting a constant $\tilde{T}_c$ from the observed total torque in each belt. The resulting fluxes $(\tilde{F}^*_h)_{ij}$ are inserted in (2.3) and the adjusted vertical fluxes $(\tilde{F}^*_v)_{ij}$ follow from (2.3) by integrating this equation vertically, assuming (2.7) at

the bottom. Moreover, (2.9) ensures $(\tilde{F}_v^*)_{iJ+1} = 0$. Note that (2.9) imposes an exact angular momentum balance for each belt, but not for each annulus. The adjusted fluxes $\tilde{F}_h^*$, $\tilde{F}_v^*$ will only be used in the budget studies. It is an unsatisfactory feature of (2.9) that the torque data are accepted as correct.

3. Results

In what follows we present first the fields $\tilde{\mu}$, $\tilde{F}_h$, $\tilde{F}_v$ and the related torques. After that, budgets will be considered and, finally, a streamfunction and a flux potential are derived.

a. Angular momentum, fluxes, and torques

The annual cycle of the total angular momentum is displayed in vector form in Fig. 2a as a function of latitude and height. The angular momentum vector in an annulus has the components $(\tilde{\mu}_c, \tilde{\mu}_s)$. The convention is such that the direction of an arrow reveals that time when the corresponding variable attains its maximum value. A horizontal vector pointing to the right indicates that this maximum occurs on 1 January; an upright vector corresponds with 1 April. The length of the vector characterizes the amplitude.

It is seen that the annual cycle of the angular momentum is weak in the Tropics, but attains amplitudes of almost 2×10^{24} Joule seconds (J s) in the subtropics. The annual variation is small for $|\varphi| > 60°$. The oscillations extend to the lower stratosphere with little variability in the vertical. Of course, the maxima are attained in the respective winter seasons. There is a slight asymmetry in that the oscillations in the Northern Hemisphere are stronger than those in the south. This feature corresponds, of course, with the observed maximum of $\hat{M}$ in the boreal winter (e.g., Oort 1989). A switch to the equal mass grid would have little effect in this case. A turn of the vectors in Fig. 2a to the right by $\pi/2$ and a multiplication by ω_a generates the corresponding tendency of the angular momentum. The maximum vector length is 0.3 Hadley (1 Hadley = 10^{18}J) in that case.

The semiannual component (Fig. 2b) is weaker than the annual one with maxima in May and November almost throughout the region $|\varphi| \leqslant 30°$, except for the lower equatorial troposphere where the peak occurs early in February and August. There is also some activity in the region $30°\text{N} \leqslant \varphi \leqslant 60°\text{N}$, but not in the corresponding domain of the Southern Hemisphere. So, while the annual oscillation is strong outside of the Tropics, the opposite is the case with the semiannual oscillation. This feature would be less pronounced in the equal mass grid.

The contribution of the mass term to Fig. 2a is shown in Fig. 3a. The annual cycle of the mass term is strongest in the lower troposphere at midlatitudes. A weaker oscillation of opposite sign is seen in the stratosphere. The annual cycle of the mass term is clearly dominant in the extratropical lower troposphere when compared to that of the wind term (Fig. 3b). Higher up, the annual cycle of the mass term is opposed to that of $\tilde{\mu}$, and it is the wind term that dominates there. The oscillation of

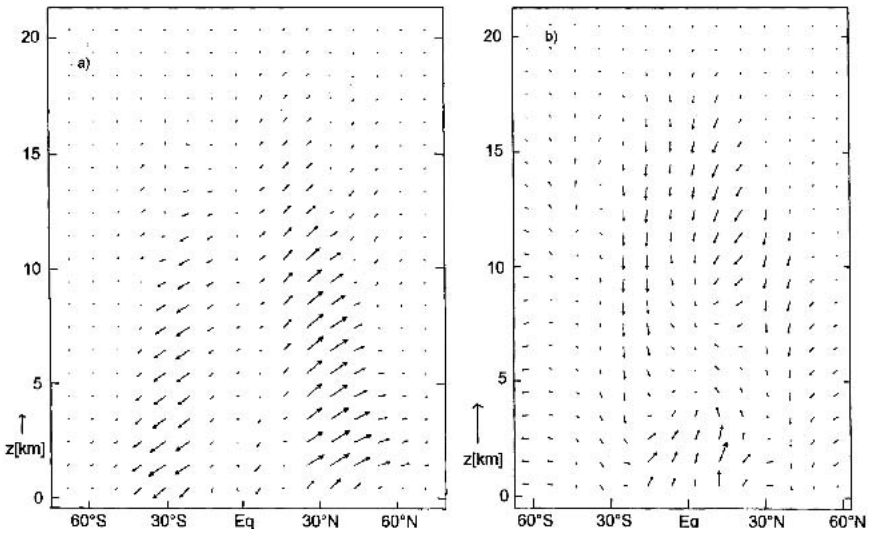

FIG. 2. (a) Annual and (b) semiannual component $\tilde{\mu}$ of the angular momentum per annulus presented as vector $(\tilde{\mu}_c, \tilde{\mu}_s)$ with a maximum vector length of 1.7×10^{24} Js in and 0.4×10^{24} Js, respectively. Here, and in all following vector plots, the horizontal component is oriented toward the right for positive values and represents the cosine component, while the sine component is oriented upward. Thus, the maximum occurs on 1 Jan for a vector pointing to the right and on (a) 1 Apr and (b) 14 Feb for an upright vector. Polar and upper domains are omitted where the vectors are too short to contain information in the display.

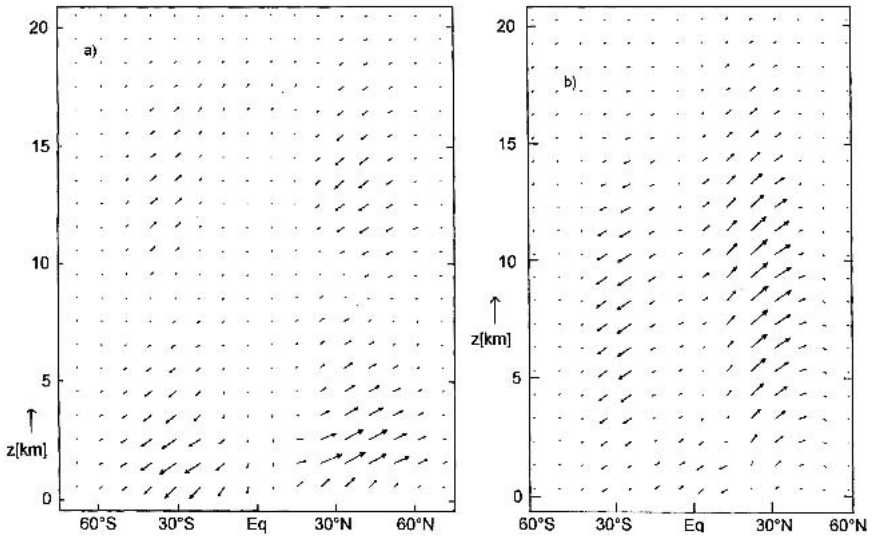

FIG. 3. Annual component (a) $\tilde{\mu}_m$ of the mass term and (b) $\tilde{\mu}_w$ of the wind term, with maximum vector lengths of 1.3×10^{24} Js and 1.4×10^{24} Js, respectively; see Fig. 2 for the definition of the vectors.

the mass term in an annulus is, of course, tantamount to an oscillation of the mass content. Hence, corresponding mass fluxes are required. It has to be kept in mind, however, that the prognostic equation

$$\frac{\partial}{\partial t}\overline{\mu}_m + \Omega a^2 \cos^2\varphi\left(\frac{1}{a}\frac{\partial}{\partial\varphi}\overline{\rho v} + \frac{\partial}{\partial z}\overline{\rho w}\right) = 0 \quad (3.1)$$

for the mass term weighs the divergence of the mass transport with $\cos^2\varphi$ so that mass shifts at low latitudes generate larger effects than those near the poles. Figure 3a implies a maximum of mass content in February in the domain $30° \leqslant \varphi \leqslant 50°$N, $0 \leqslant z \leqslant 6$ km, say. This increase of density during winter is, of course, also contained in the early analyses of Oort and Rasmusson (1971).

The distribution of the wind term's annual cycle is presented in Fig. 3b. The observed zonal wind maximum near 30°N late in winter is the dominant feature in the Northern Hemisphere, with corresponding but weaker oscillations in the south. The basic structure of Fig. 3b resembles closely that of Fig. 3 of Huang and Sardeshmukh (2000). However, the wind term is small in the lower troposphere in Huang and Sardeshmukh (2000; see also Fig. 10 of Rosen et al. 1987) because the decrease of density with height is not reflected in pressure coordinates. The pattern in Fig. 2a is a superposition of Figs. 3a and 3b, where both the wind and the mass terms are important. The semiannual component of the wind term (not shown) contributes most of the features in Fig. 2b (see also Fig. 4 of Huang and Sardeshmukh 2000), except for the lower equatorial troposphere where the mass term is again dominant.

The annual cycle of the horizontal fluxes is displayed in Fig. 4 where the transports of mass and wind terms are presented separately. As for the mass term (Fig. 4a), the seasonal oscillations of the fluxes are largest by far in the Tropics. There is a shallow layer of transports close to the ground with opposite fluxes aloft due to the seasonal shift of the Hadley cell (Oort and Rasmusson 1971; PO). A maximum flux of 210 Hadley, as in Fig. 4a, corresponds with a mass flux of 1790 kg m^{-1} s^{-1} at the equator or a mean meridional velocity of 1.8 m s^{-1} in the corresponding layer, if we assume a density of 1 kg m^{-3}.

Although there is substantial cancellation of the mass transports in the upper and lower troposphere in Fig. 4a, the vertically integrated fluxes of angular momentum linked to the mass term are up to 80 Hadley in the equatorial belt to become quite small for $|\varphi| = 30°$. These large mass fluxes near the equator are spurious. The maximum of 55 Hadley at the equator implies a total mass flux of 466 kg s^{-1} m^{-1}, with a corresponding vertically averaged meridional velocity of 0.05 m s^{-1}. This is much more than the maximum velocity of 2–3 $\times$ 10^{-3} m s^{-1} found by PO, who estimated the flux on the basis of the annual oscillation of the hemispheric mean surface pressure. Hoinka (1998) arrived at a similar value when repeating these calculations with the ERA surface pressures. In principle, an error of ~0.05 m s^{-1} is quite small in an analysis system, but is by far too large to be tolerable here. However, the adjusted cross-equatorial flux with a maximum velocity of 6×10^{-3} m s^{-1} is reasonably close to that of the observations.

The fluxes related to the mass term are about two orders larger than those of the wind term (Fig. 4b). The well-known maximum of northward momentum transports that occur late in boreal winter near 30°N is seen quite clearly in Fig. 4b, as well as is the corresponding

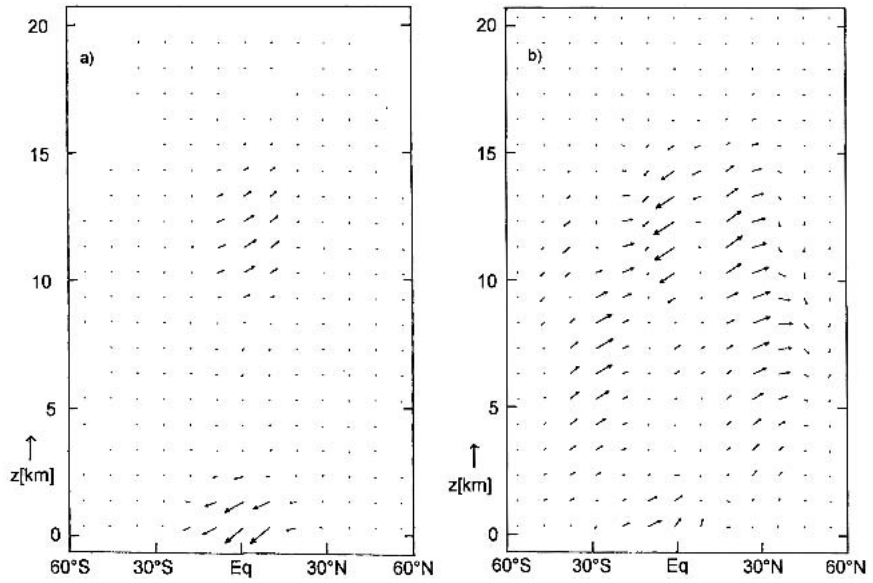

FIG. 4. Annual components $\tilde{F}_h$ of the horizontal flux of angular momentum: (a) mass term with a maximum vector length of 210 Hadley, and (b) wind term with a maximum vector length of 2.7 Hadley; see Fig. 2 for the definition of the vectors.

feature in the Southern Hemisphere. The narrow zone of strong southward transports in February above the equator is a novel feature. A separation in wind and mass term fluxes is not possible for the adjusted fluxes, but the adjusted fluxes (not shown) are so similar to those in Fig. 4a that differences would not be visible.

The annual components of the vertical transport $\tilde{F}_v$ as resolved by the analysis scheme are presented in Fig. 5. Again, it is in the Tropics that the fluxes of the mass term are strong. Positive fluxes peak in March in the Southern Hemisphere, and about half a year later in the north. This pattern reflects the annual shift of the Hadley cell (e.g., PO). Of course, it is again the transport linked to the mass term that is, by far, larger than that of the wind term that is seen in Fig. 5b. The vertical flux vectors of the wind term (Fig. 5b) are opposite to

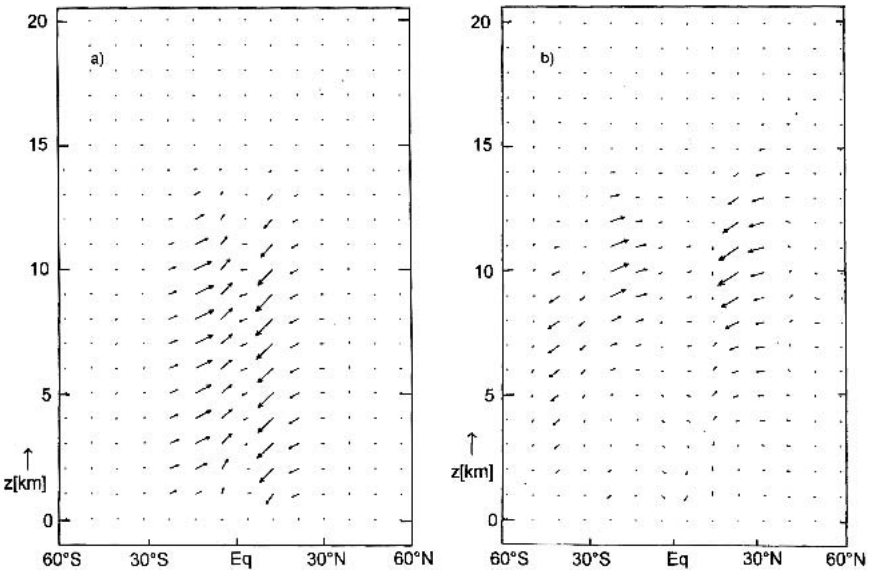

FIG. 5. Annual components $\tilde{F}_v$ of the resolved vertical flux of angular momentum: (a) mass term with a maximum vector length of 320 Hadley, and (b) wind term with a maximum vector length of 5.7 Hadley; see Fig. 2 for the definition of the vectors.

the horizontal transports in the upper troposphere near 30°N (see also Hantel and Hacker 1978). The strong and important positive transport of the wind term in winter is coupled to an even stronger negative vertical flux. It is the same near 30°S. The fluxes of the semiannual component are not shown for the sake of brevity. A shift to the equal mass grid would affect $\tilde{F}_v$, but not $\tilde{F}_h$.

Note that the vector fields in Figs. 2–5 are smooth, at least in general. Therefore, the chosen resolution of $D_\varphi = 9°$ is sufficient to capture the salient features of the various annual cycles. On the other hand, there are noisy structures in the lower equatorial troposphere in Fig. 5b. However, the related fluxes are quite weak.

The adjusted flux $\tilde{F}_v^*$ differs from the resolved flux at the ground where $\tilde{F}_v^*$ equals the torque, while F_v vanishes there. Otherwise, the fluxes linked to the torques are dwarfed by the mass fluxes. It is, therefore, better to represent the torques separately.

The seasonal cycle of the torques is shown in Fig. 6 for all of the belts. The vector arrays are quite noisy despite the relatively coarse resolution $D_\varphi = 9°$. Clearly, the annual cycle of the friction torque dominates. The strongest contributions to $\hat{T}_f$ are related to the trade winds, with maximum positive fluxes in August and September in the Southern Hemisphere and in the boreal spring in the Northern Hemisphere (see also Fig. 11.11 of PO). Outside of the Tropics the friction torque peaks late in the austral summer when the surface westerlies are weakest. The situation is more complicated in the Northern Hemisphere where peaks are found also in fall. The oscillations of the mountain torque are smaller than those of the friction torque, but nevertheless are important for $|\varphi| \leqslant 40°$ (see also Madden and Speth 1995). The maxima are mostly attained in fall in the Northern Hemisphere. The tropical mountain torques peak in the respective winter season (e.g., Oort 1989). The oscillation of the gravity wave torque has an amplitude that is comparable to that of the mountain torque itself. For example, the amplitude of the gravity wave torque is 4 Hadley in belt $i = 15$ ($\hat{\varphi} = 40.5°$N), where that of the mountain torque is just 2 Hadley. Although the mountain torque is somewhat larger than the gravity wave torque in most of the other belts, it is clear that the parameterization of the gravity wave drag torque overestimates $\hat{T}_g$. This result complements that of Huang et al. (1999), who obtained unrealistic results for the gravity wave torque in the National Centers for Environmental Prediction (NCEP) data. Therefore, $\hat{T}_g$ will be excluded in the following more quantitative analysis. A switch to the equal mass grid would, of course, not only affect the position of the grid points, but reduce the tropical torques by a factor ~0.6. The torques in the polar cap would remain quite small. This does not mean that they are unimportant because the fluxes and angular momenta are small there as well.

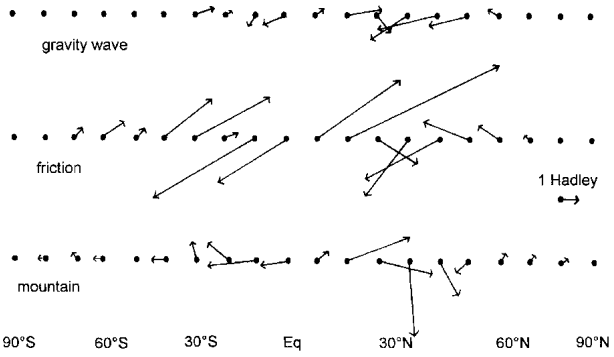

FIG. 6. Annual components of the mountain, friction, and gravity wave torque. The dots give the meridional location of the centers of the 20 belts. Vectors below drawing accuracy are omitted; see Fig. 2 for the definition of the vectors.

b. Budgets

The angular momentum Eq. (1.1) has been cast in the form (2.3), which is suitable for budget studies. We have to choose budget domains in contact with the ground if we want to elucidate the role of the torques. Of course, the global atmosphere satisfies this requirement. The amplitude of the global angular momentum tendency is just 3.8 Hadley with a phase of −58° so that the maximum tendency occurs late in October, in agreement with earlier work (e.g., Oort 1989, see his Fig. 8). The corresponding amplitude of the sum of friction and mountain torque is 4.4 Hadley with a phase of −11°. The contribution of $\hat{T}_f$ is slightly larger than that of the mountain torque. Thus, the agreement of the amplitudes is almost perfect and the phases differ just by ~45 days. Note that a total torque amplitude of 4 Hadley is a small residual given the large contributions by individual belts as shown in Fig. 6. An incorporation of the gravity wave drag with an amplitude of 8 Hadley would destroy this good result. The total semiannual torque without T_g is 4.3 Hadley with a phase of 152°. This torque fits quite well the observed tendency of 5.3 Hadley with a phase of 153°. The global mountain torque has almost twice the amplitude of the friction torque for the semiannual component. Again, the gravity wave torque would degrade the result. Although the semiannual global torque has a slightly larger amplitude than the annual torque, the contributions by the individual belts (not shown) are relatively small, with a maximum of 3 Hadley (belt 12), as compared to 16 Hadley (belt 12) for the annual component. As is well known (e.g., Huang and Sardeshmukh 2000), the annual and semiannual angular momenta are almost out of phase, so that the annual minimum of the total angular momentum M in July is more pronounced than the maxima in boreal winter and spring.

In general, we have to sum (2.3) over the control domains spanning the belts $i_1 - i_2$ and the layers $j_1 - j_2$. Then, we find from (2.3)

$$\sum_{ij} (i\omega_a \tilde{\mu}_{ij}) = -\sum_{i} [(\tilde{F}_v)_{ij_2+1} - (\tilde{F}_v)_{ij_1}] - \sum_{j} [(\tilde{F}_h)_{i_2 j} - (\tilde{F}_h)_{i_1-1 j}], \quad (3.2)$$

where i runs from i_1 to i_2 and j from j_1 to j_2. In particular, the vertical flux for $j_1 = 1$ is identical to the sum of mountain and friction torque. The first term in (3.2) is the tendency. To demonstrate the need for flux adjustment, we choose $j_1 = 1$ and lump all flux terms together on the right of (3.2) to form the sum of the total torque $\tilde{T}$ and the total flux $\tilde{F}$. That is, the "forcing" must balance the tendency. We present in Fig. 7 the torque and transport, as well as the tendency vector, for two domains extending over the full depth of the analysis domain. The Southern Hemisphere's torque of 12 Hadley peaks in the austral winter, the unlabeled tendency of 8 Hadley attains its maximum late in the fall. The contribution by the fluxes is quite large and peaks in February so that the forcing $\tilde{T} + \tilde{F}$ deviates considerably from the tendency. These large transports represent the spurious cross-equatorial mass transports mentioned above. In other words, we have to replace $\tilde{F}$ by the adjusted flux $\tilde{F}^*$. By definition, the sum of $\tilde{F}^*$ and $\tilde{T}$ balances the tendency vector in Fig. 7 [see (2.9)]. The amplitude $|\tilde{T}|$ of the torque vector is larger than that of the adjusted transport vector. The tendency is somewhat larger in the Northern Hemisphere (not shown), as is the torque, so that the relative importance of the torques is even stronger than in the south. As a second example, we show in Fig. 7 the angular momentum balance for the midlatitude domain of the Northern Hemisphere. Again, the contribution $\tilde{F}$ by the fluxes is too large given the torque and the tendency. A closer inspection shows that the flux from the south is too strong in this case. The corrected flux $\tilde{F}^*$ has about the same orientation as $\tilde{F}$ but is, of course, much weaker. Altogether, it is clear from these examples, that the fluxes as provided by the ERA must be replaced by adjusted fluxes if we want to perform budget studies.

Let us now consider a few domains in more detail. Results are presented in Figs. 8–9 for the polar caps and midlatitude domains. The mass contained in the latter is about 4 times that within the polar cap. For all domains (dashed rectangles), the corrected transports are split into horizontal contributions (northward, right; southward, left) and vertical components (top and bottom of rectangle). The torque $\tilde{T}$ is represented at the bottom of a rectangle if $j_1 = 1$. The tendency is given in the center of each rectangle. The convention is such that the sum of all of the vectors at the boundaries of a domain equals the tendency in the center so that the contributions of transports and torques to the tendency can be visualized easily.

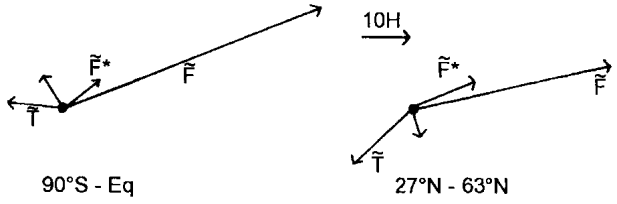

FIG. 7. Angular momentum budget of the annual cycle for the (left) Southern Hemisphere and for the (right) northern midlatitudes. The vectors per domain are the sum $\tilde{T}$ of mountain and friction torque, the sum $\tilde{F}$ of all flux vectors, the unlabeled tendency, and the adjusted flux $\tilde{F}^*$. The sum of $\tilde{T}$ and $\tilde{F}^*$ equals the tendency. The depth is $H = j_2 D_z = 28$ km. Also given is the scaling of the vectors.

The torque in the Antarctic domain peaks in the austral winter when the surface easterlies are strongest (Fig. 8, left). Its contribution to the budget of the Antarctic lower troposphere (Fig. 8; $0 \leq z \leq 5$ km) is partly balanced by the tendency. But, most of the angular momentum transferred to the domain from below is exported to the upper troposphere and even to the stratosphere. The orientation of the horizontal fluxes in the lower troposphere is opposite to that of the vertical transports. These fluxes represent mainly mass transports. It has been argued by Egger (1992; see also Juckes et al. 1994) that the angular momentum gained through the positive annual mean of the friction torque in Antarctica is transported to the upper troposphere to be transported toward the midlatitudes by topographically modified Rossby waves. Moreover, Juckes et al. (1994) demonstrated, on the basis of model-generated data, that mass fluxes are important in the momentum balance of Antarctica. Figure 8 demonstrates that these results apply equally well to the annual cycle. It is seen, in addition, that the stratosphere plays an important part in this budget. The tendency in the domain $15 < z < 28$ km is too small to be drawn in Fig. 8, but the fluxes reach amplitudes of more than 1 Hadley with maximum impact from below in the austral spring, that is, when the stratospheric vortex decays.

The torque in the northern polar cap (Fig. 8, right) is quite small and peaks in the winter. The torque is oriented almost normal to the tendency in the lowest domain and is mainly balanced by the horizontal fluxes. Vertical fluxes are important and balance, inter alia, the tendency in the intermediate domain. As in Antarctica the upper, completely stratospheric domain is important.

The dominating feature of both of the budgets of the midlatitude belts is the large fluxes from and to the Tropics, with a strong corresponding vertical flux component between the lowest and the intermediate box. A look at Figs. 4 and 5 reveals that fluxes of the mass term are the main contributors. The projection of the torques on the tendency in the lowest domain is positive in the south, but vanishes almost in the north where the tendency is a rather small residual of the fluxes. It is difficult, if not impossible, to explain the tendency in terms of the fluxes because the nondivergent component of the fluxes is so large (see also section 3c). The

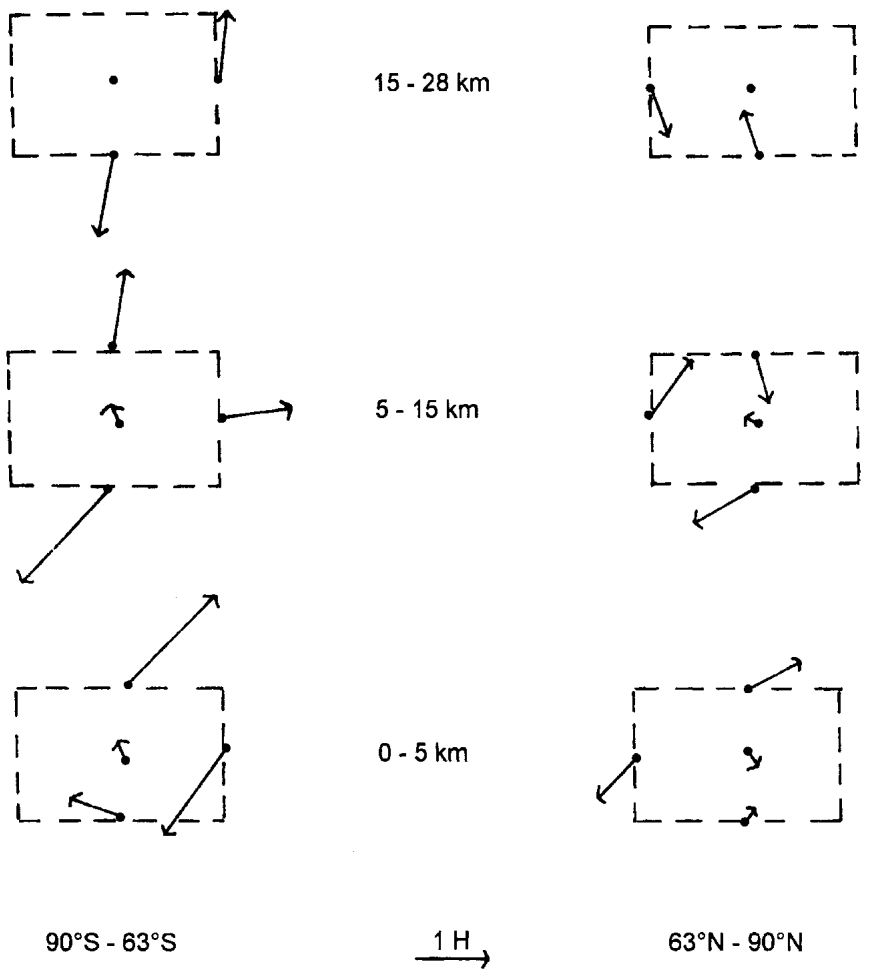

FIG. 8. Angular momentum budgets of the annual cycle of the polar domains: (left) 90°–63°S, belts 1–3; and (right) 63°–90°N, belts 18–20. The dashed rectangles represent the domains and the vectors at the boundaries are the contributions by the respective corrected fluxes. In particular, the vector at the bottom of the lowest domain is the torque $\tilde{T}$. The convention is such that the vectors at the boundaries add up to the tendency vector at the center of a domain. The height extension of the domains is given in the center, as is the scaling.

relative importance of the stratosphere is not as large as in the polar domains but is still surprising.

The budgets of the tropical domains are fairly good mirror images of each other (not shown). For example, the flux from above into the lower troposphere of the Northern Hemisphere domain peaks in February with 335 Hadley, while that in the south reaches its maximum of 366 Hadley half a year later. Clearly, these enormous transports are essentially due to the fluxes of mass. Both the tendency and the torques are dwarfed by these huge fluxes.

c. Streamfunction and flux potential

The dominance of the nondivergent part of the fluxes in the budgets suggests the introduction of the well-known concepts of streamfunction φ and flux potential χ to achieve a separation of divergent and nondivergent fluxes. Any two-dimensional flux **F** can be written

$$\mathbf{F} = \nabla\chi + \mathbf{n}x\nabla\psi \tag{3.3}$$

(**n** unit vector is perpendicular to the meridional plane). Here, integrated functions $\tilde{\psi}_{ij}$, $\tilde{\chi}_{ij}$ are introduced, which are defined in the analysis grid (see Fig. 1b). Thus, (3.3) is converted to

$$\begin{aligned}(F_h^*)_{ij} &= \tilde{\psi}_{i+1j+1} - \tilde{\psi}_{i+1j} + \tilde{\chi}_{i+1j} - \tilde{\chi}_{ij},\\ (F_v^*)_{ij} &= \tilde{\psi}_{i+1j} - \tilde{\psi}_{ij} + \tilde{\chi}_{ij} - \tilde{\chi}_{ij-1}.\end{aligned} \tag{3.4}$$

Note that the gridpoint field $\tilde{\psi}_{ij}$ is normalized with respect to distances, as is $\tilde{\chi}_{ij}$. The streamfunction vector $\tilde{\psi}$ represents the rotational, nondivergent part of the flux, which is oriented tangentially to the streamlines. The angular momentum is not affected by this part of the flux. The potential $\tilde{\chi}$ captures the divergent part of the flux, which is oriented normal to the isolines of the potential. Streamfunctions were calculated by PO for

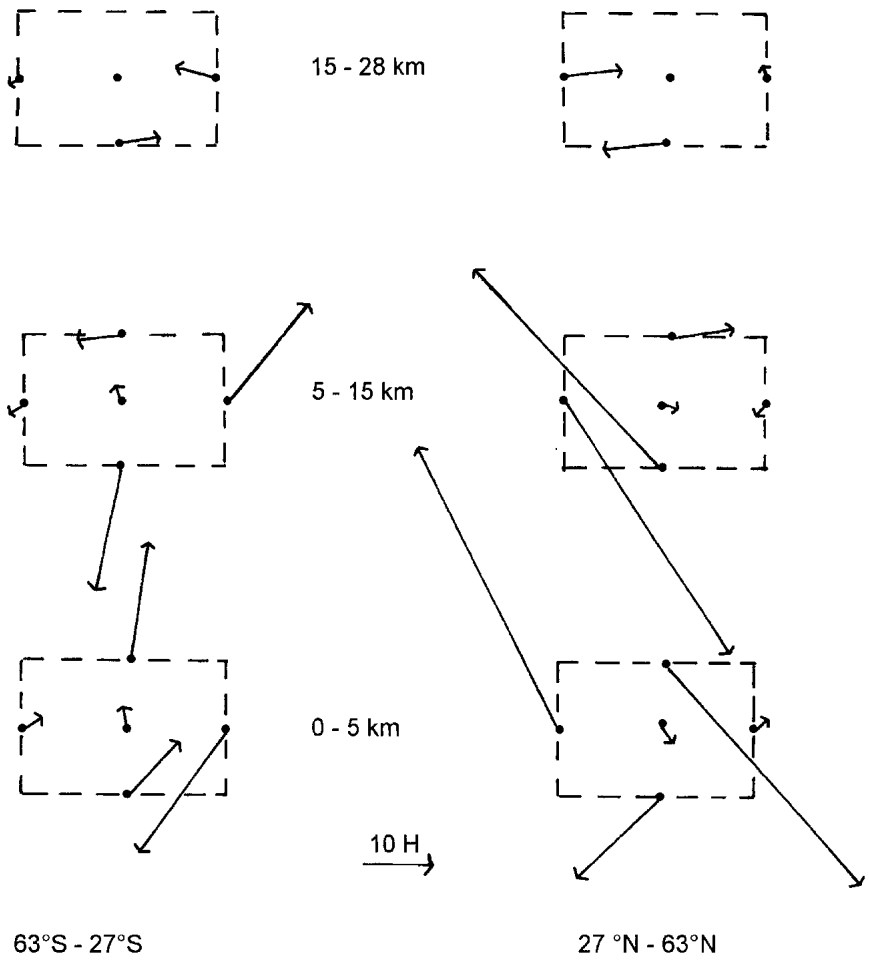

FIG. 9. Annual angular momentum budgets of the annual cycle of the midlatitude belts: (left) 63°–27°S, belts 4–7; and (right) 27°–63°N, belts 14–17. Otherwise, the same as in Fig. 8.

the seasonal transports of the angular momentum while a flux potential has not been presented as yet. The "vorticity" $\nabla^2\psi$ becomes

$$-4\tilde{\psi}_{ij} + \tilde{\psi}_{i+1j} + \tilde{\psi}_{i-1j} + \tilde{\psi}_{ij+1} + \tilde{\psi}_{ij-1} = (\tilde{F}^*_v)_{ij} - (\tilde{F}^*_v)_{i-1j} - (\tilde{F}^*_h)_{i-1j} + (\tilde{F}^*_h)_{i-1j-1} \quad (3.5)$$

in the grid. This equation must be solved for $\tilde{\psi}_{ij}$ with $\tilde{\psi}_{1j} = \tilde{\psi}_{I+1j} = \tilde{\psi}_{iJ} = 0$. The flow potential is a solution to $\partial/\partial t\ \overline{\mu} + \nabla^2\chi = 0$, that is,

$$i\omega_a\tilde{\mu}_{ij} + \tilde{\chi}_{ij+1} + \tilde{\chi}_{ij-1} + \tilde{\chi}_{i+1j} + \tilde{\chi}_{i-1j} - 4\tilde{\chi}_{ij} = 0, \quad (3.6)$$

with $\tilde{\chi}_{0j} = \tilde{\chi}_{1j}$, $\tilde{\chi}_{I+1j} = \tilde{\chi}_{Ij}$, $\tilde{\chi}_{iJ+1} = \tilde{\chi}_{iJ}$. Note that the observed tendencies do not affect the streamfunction. To specify both $\tilde{\psi}$ and $\tilde{\chi}$ at $z = 0$, we have to calculate the contribution of a belt's torque to the total tendency in that belt. Thus, if

$$\tilde{d}_i = \sum_{j=1}^{J} i\omega_a\tilde{\mu}_{ij} \quad (3.7)$$

is the total tendency of belt i, the contribution of the torque $\tilde{T}_i$ to (3.7) is

$$\tilde{T}_{di} = \tilde{T}_i(\tilde{T}_i \cdot \tilde{d}_i)\,|T_i|^{-2}, \quad (3.8)$$

where the scalar product of the vector $\tilde{T}_i$ and $\tilde{d}_i$ in (3.8) is defined as usual. Of course, (3.8) is a formalization of Fig. 7, where the torque and the transports add up to the tendency. The projection (3.8) captures that part $\tilde{T}_d$ of the torque that affects the tendency in that belt. It must, therefore, be attributed to the velocity potential, while the part $\tilde{T}_i - \tilde{T}_{di}$ has no impact on the tendency and is, therefore, attributed to the streamfunction. Hence, we prescribe

$$\tilde{\psi}_{i+11} - \tilde{\psi}_{i1} = \tilde{T}_i - \tilde{T}_{di} - \tilde{C} \quad (3.9)$$

at the lower boundary, where the choice

$$\tilde{C} = \sum_{i=1}^{I} (\tilde{T}_i - \tilde{T}_{di}) \quad (3.10)$$

ensures that the summation of (3.9) over all of the belts gives $\tilde{\psi}_{I+11} = 0$. It follows that

$$\tilde{\chi}_{i2} - \tilde{\chi}_{i1} = \tilde{T}_{di} + \tilde{C} \tag{3.11}$$

at the lower boundary. The evaluation of the ratio $R = |\tilde{T}_{di} + \tilde{C}|/|\tilde{T}_i - \tilde{T}_{di} - \tilde{C}|$ shows that the relative impact of the torques on the tendency may be large at the poles and midlatitudes, where $0.1 \leqslant R \leqslant 1.1$, but small in the trade winds belts (9–12) with $R \leqslant 0.1$.

The streamfunction for 1 January is shown in Fig. 10a, that for 1 April is shown in Fig. 10b. Both patterns are, of course, completely dominated by the mass circulation of the Hadley cell (see also PO), which is anticyclonic in both cases, in agreement with Figs. 4 and 5. The vertical extent of the cell is ~15 km, and there is a slight asymmetry (as in Fig. 5a) in that the descending branch tends to be more narrow than the ascending branch in the south. The circulation in April is somewhat weaker than in January. The impact of the lower boundary condition is obviously small. It is only a few streamlines that intersect the ground. Note that streamlines emerging from the ground have to return to it, except if $\tilde{\psi} = 0$ on the streamline. The $\tilde{\psi}$ pattern for 1 February is similar to that in Fig. 10a, but the circulation is slightly more intense. On the other hand, the cyclonic cell in the Northern Hemisphere on 1 May is almost as strong as the equatorial anticyclonic cell, but maximum amplitudes are as low as 5 Hadley.

The flux potential is displayed in Fig. 11. In the winter there is a maximum of $\tilde{\chi}_c$ in the northern tropical latitudes at a height of ~8 km. Tendencies are positive in this area (see Fig. 2a) and, correspondingly, the divergent part of the transports is directed toward the maximum as a center of convergence. The annual march of the Hadley cell is not completely described by Fig. 10, but involves also changes of the angular momentum. At the lower boundary there is a minimum of $\tilde{\chi}_c$ underneath this maximum, but it is shifted slightly southward. This minimum represents the impact of the torques. Its amplitude is more than twice that of the maximum at the surface in the south. The amplitude of

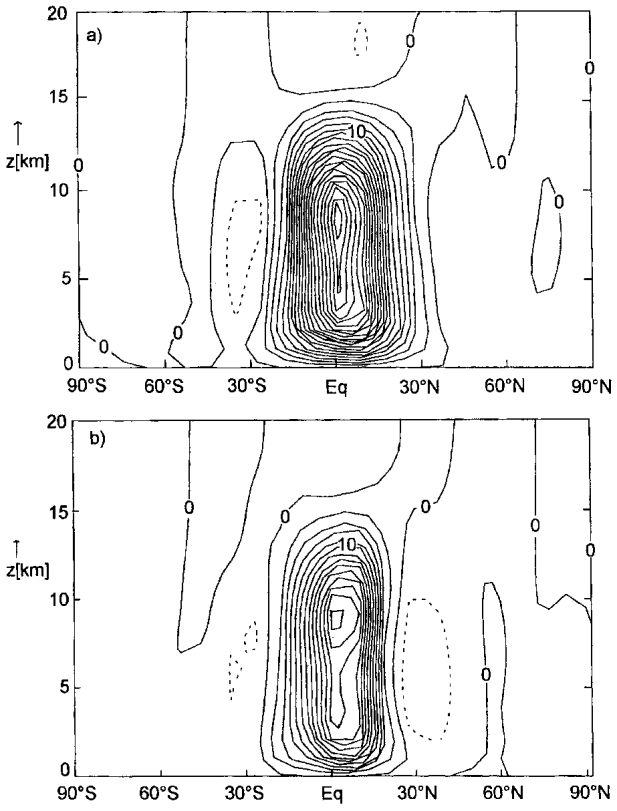

FIG. 10. Streamfunction $\tilde{\psi}$ (10 Hadley) of the annual cycle angular momentum transport for (a) 1 Jan ($\tilde{\psi}_c$) and (b) 1 Apr ($\tilde{\psi}_s$), with a maximum value in the center of the equatorial cell of 420 and 271 Hadley, respectively. Presentation restricted to heights $z \leq 20$ km. Contour interval 20 Hadley.

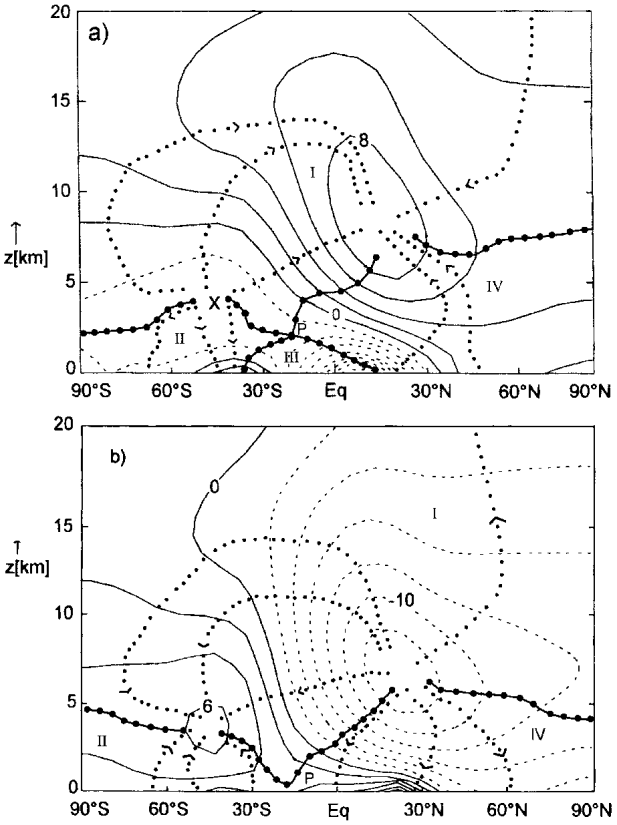

FIG. 11. Flux potential $\tilde{\chi}$ (0.1 Hadley) of the annual cycle of the angular momentum for (a) 1 Jan ($\tilde{\chi}_c$) and (b) 1 Apr ($\tilde{\chi}_s$); trajectories (dotted), separatrices (dash dots), and saddle point *P*. The X in (a) marks the location of the minimum of −3.9 Hadley. The contour interval is 0.2 Hadley. Presentation for heights $z \leqslant 20$ km. Trajectories and separatrices are not drawn close to the centers of convergence/divergence. Moreover, the gridpoint representation is too coarse to allow for a reasonably accurate evaluation near such points. The reentry of the "stratospheric" trajectory into the domain of presentation in (a) has not been calculated because of the uncertainty of the flux data at upper levels. Negative isolines are dashed.

the annual cycle and, therefore, that of its tendency in the Southern Hemisphere is smaller, and the related minimum is located (cross in Fig. 11a) at lower heights than the maximum in the north (see also Fig. 2a). There is a saddle point P close to the ground near 20°S, which separates the two maxima and the two minima. Maximum horizontal fluxes are ~0.4 Hadley near the equator. If these fluxes were entirely due to mean meridional mass transports $\hat{v}\rho$, the corresponding flux velocities were $\leqslant 10^{-2}$ m s^{-1}.

The dotted lines in Fig. 11 are "trajectories" of the divergent flow. These trajectories follow the flux vector $(\nabla\tilde{\chi})$ of the divergent part of the fluxes in the (φ, z) plane, just as trajectories in the airflow follow the wind. They are orthogonal to the isolines of $\tilde{\chi}$. The direction of a trajectory as indicated by the arrowheads in Fig. 11 is that of the gradient. It does not indicate causality. However, we can establish close relations between tendency, torques, and transports by integrating (3.6) over budget areas Q. Thus, one obtains

$$\int_Q \omega_a \mu_s df + \oint_S \nabla\tilde{\chi}_c \cdot \mathbf{n} ds = 0 \tag{3.12}$$

for the winter season where S is the boundary of Q with unit vector $\mathbf{n}$ oriented normal to it. To exploit (3.12) we will consider only areas Q where S consists of trajectories and/or parts of the ground. Of course, there is no contribution to the second integral whenever S is part of a trajectory. The dash-dotted lines in Fig. 11 are the separatrices, which separate the "basins of influence" of the torques and of the extrema of the tendency. They have been determined approximately by calculating a great number of trajectories. Curves that are not crossed by trajectories are separatrices. There is a separatrix that connects the southern boundary with the minimum and the saddle point. Another one leads from P via the maximum to the polar boundary. Two more separatrices link P with the surface. Domain I is located above all of the separatrices. Control surfaces in domain I are confined by pairs of trajectories emerging from the minimum and joining again at the maximum so that

$$\int_Q \omega_a \mu_s df = 0. \tag{3.13}$$

There is no mean tendency in areas enclosed by pairs of trajectories. In other words, the torques do not affect the annual cycle in domain I. However, angular momentum flows toward the maximum within Q. The related flux pattern is interhemispheric. Domain II contains the lower troposphere of Antarctica and the southern midlatitudes. It is not possible to construct control surfaces in domain II that are confined by trajectories only. Instead, the boundary S contains part of the ground. Therefore, the torques affect the tendency throughout domain II. Domain III is small and located underneath the saddle point. Trajectories emerge from the ground and return to it in domain III. They cannot reach any of the two extrema. Such trajectories are not drawn in Fig. 11a, because domain III is represented by a few grid points only. This implies considerable uncertainty with respect to the calculation of trajectories. In any case, the torques in domain III act on fairly shallow layers only. Domain IV is the northern analog of domain II, but is deeper and meridionally more extended. The torques affect the atmosphere in domain IV.

In April (Fig. 11b), signs are opposed to those in January. There is a minimum in the Northern Hemisphere indicating the decrease of $\tilde{\mu}$ (see Fig. 2a). The saddle point is so close to the ground that a domain III does not exist in April. Otherwise, the situation is fairly similar to that in January, except that both extrema are stronger than in winter. Domain IV is again more extended than domain II, a feature that reflects the impact of the mountains.

The winter regime in Fig. 10a fades fairly quickly. The velocity potential pattern for 1 February contains hardly any features above the lower troposphere. The structures in Fig. 10b are found also 1 month late, but with increased amplitudes.

Given Fig. 11, we may turn back to the budgets presented in Figs. 8 and 9. As for the polar domains, we can state that the tendency in the lower Antarctic troposphere is strongly affected by the torques, while the large fluxes on top do not contribute to the tendency of that domain. The annual cycle of $\overline{\mu}$ in the intermediate domain ($5 \leqslant z \leqslant 15$ km) is, however, not affected by the torques, but reflects the convergence of fluxes of planetary scale. In the Arctic, the impact of the torques extends also to the lower troposhere only. The tendency in the lower polar troposphere in the Northern Hemisphere results mainly from fluxes linked to the extremum of $\tilde{\chi}$.

4. Conclusions and discussion

Earlier studies of the annual cycle of the axial angular momentum have been extended in this paper on the basis of the ERA by deriving a consistent set of angular momentum tendencies, of horizontal and vertical transports and of the related torques. The analysis has been performed in height coordinates so that the information on the mass term is on equal terms with that on the wind term.

It is found that the annual cycle of the mass term is larger than that of the wind term in the lower troposphere. The related transports due to the annual shift of the Hadley cell are much more intense than those of the wind term. The global budgets revealed good agreement of the observed global angular momentum tendency with the sum of the global mean mountain and friction torque as observed both for the annual and the semiannual components. This agreement is lost if the

gravity wave drag is added. The analysis of specific regions showed a substantial cancellation of the contributions of the torques and the transports on the angular momentum tendency for deep domains. The pattern of the streamfunction of the fluxes is dominated by the signatures of the Hadley circulation, while that of the flux potential has an extremum in each hemisphere. The impact of the torques on the annual cycle of the angular momentum extends to the lower troposphere only. The related heights of influence are a few kilometers in the Tropics, 4–5 km in Antarctica and the southern midlatitudes, and 3–7 km in domain IV. Higher up, an interhemispheric flux pattern imposes the tendencies.

The statistical significance of our results is of concern. Fourteen years of observations may not be enough to deal with eventually noisy factors like the torques. To address this point, the contribution of individual years to the torques in a belt have been evaluated so that standard deviations σ_a of amplitudes and phases (σ_p) are available. The standard deviations of the phases of the friction and mountain torque are displayed in Fig. 12. The interannual variation of the friction torques is quite small for $|\varphi| < 45°$. In particular, the annual oscillation of the tropical torque is essentially the same from year to year where, also, the standard deviation of the amplitudes is less than 10% of the mean amplitude. The situation is quite different near the polar caps where the fluctuations from year to year are quite large. In particular, $\sigma_p = 130°$ in belts 4 and 5. Almost the same can be said with respect to the mountain torque, except for the peak of variability in belt 13, where $\sigma_p = 91°$. We have to conclude that our angular momentum budgets for, say, $|\varphi| > 45°$ are presumably subject to sampling errors. On the other hand, the annual cycle of μ has a small amplitude in these latitudes anyway so that it can be stated that our results are reliable in the regions where the annual oscillation of the angular momentum is large.

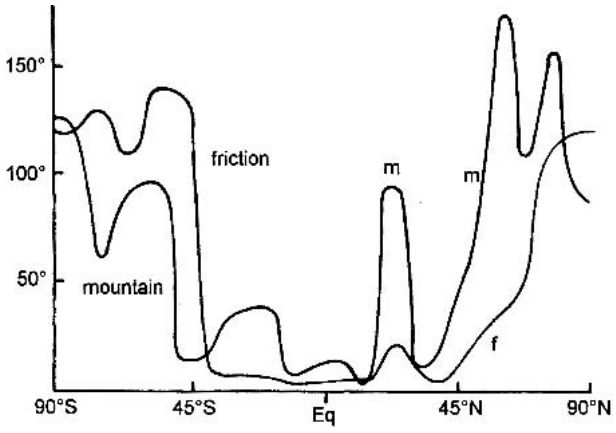

FIG. 12. Standard deviation σ_v in degrees for the phases of the annual oscillation of the friction and mountain torque per belt.

Acknowledgments. We are grateful to all three referees for their constructive criticism.

APPENDIX

Adjustment of Horizontal Transports and Torques

Let us denote the adjusted horizontal fluxes by $\tilde{F}^*_{ij}$, thus, suppressing the subscript h. We wish to minimize

$$E = \sum_{ij} (\tilde{F}^*_{ij} - \tilde{F}_{ij})^2 + \sum_i \lambda_i \Big[\sum_j (\tilde{F}^*_{ij} - \tilde{F}^*_{i-1j} + i\omega_a \tilde{\mu}_{ij}) - \tilde{T}_i \Big], \tag{A.1}$$

where $\tilde{F}_{ij}$ stands for the observed horizontal fluxes and λ_i are Lagrangian multiplicators that help satisfy the constraints of a vanishing vertical flux on top. Moreover, the observed torque at the bottom is represented this way. The sums in (A.1) run over all of the annuli. Of course, (2.9) is fulfilled automatically if E is minimized. Differentiation of (A.1), with respect to $\tilde{F}^*_{ij}$ yields,

$$2(\tilde{F}_{ij} - F_{ij}) + \lambda_i - \lambda_{i+1} = 0. \tag{A.2}$$

Combining (A.5) and (2.9), we obtain

$$2\lambda_i - \lambda_{i-1} - \lambda_{i+1} = 2I_i/J, \tag{A.3}$$

where

$$I_i = \sum_j (i\omega_a \tilde{\mu}_{ij} + \tilde{F}_{ij} - \tilde{F}_{i-1j}) - \tilde{T}_i \tag{A.4}$$

is the imbalance of the observations summed over all of the layers of belt i. Of course, I_i is known from the observations. In belt 1, (A.3) must be replaced by

$$\lambda_1 - \lambda_2 = 2I_1/J, \tag{A.5}$$

so that the difference $\lambda_1 - \lambda_2$ can be calculated. Proceeding toward the northernmost belt, we are able to evaluate all of the differences $\lambda_{i+1} - \lambda_i$ and, therefore, the necessary corrections $\tilde{F}^*_{ij}$ to the fluxes $\tilde{F}_{ij}$ [see (A.2)]. This procedure works only if

$$\sum_i I_i = 0; \tag{A.6}$$

that is, if

$$\sum_{ij} i\omega_a \tilde{\mu}_{ij} = \sum_i \tilde{T}_i. \tag{A.7}$$

To achieve this exact balance in (A.7) we subtract from the observed total torque a corresponding constant that is distributed equally over all of the belts. These corrections are small. For example, the correction of the total torque per belt is 0.16 Hadley. Finally, the vertical flux is obtained by integrating (2.3) downward from the top layer $j = J + 1$. Note that the correction does not depend on height. The adjustment procedure, as outlined, is similar in spirit to that of Hantel

and Hacker (1978), but is not restricted to the vertical transports.

REFERENCES

Egger, J., 1992: Topographic wave modification and the angular momentum balance of the Antarctic troposphere. *J. Atmos. Sci.,* **49,** 327–334.

——, and K.-P. Hoinka, 2004: Axial angular momentum: Vertical fluxes and response to torques. *Mon. Wea. Rev.,* **132**, 1294–1305.

Gibson, R., P. Kållberg, S. Uppala, A. Hernandez, A. Nomura and E. Serrano, 1997: ERA description. ECMWF Reanalysis Project Report Series, Vol. 1, 86 pp. [Available from ECMWF, Shinfield Park, Reading RGU 9AX, United Kingdom.]

Hantel, M., and J. Hacker, 1978: On the vertical transports in the northern atmosphere 2. Vertical eddy momentum transport for summer and winter. *J. Geophys. Res.,* **83** (C3), 1305–1318.

Hide, R., J. Dickey, S. Marcus, R. Rosen, and D. Salstein, 1997: Atmospheric angular momentum fluctuations during 1979–1988 simulated by global circulation models. *J. Geophys. Res.,* **102,** 16 423–16 438.

Hoinka, K.-P., 1998: Mean global surface pressure series evaluated from ECMWF reanalysis data. *Quart. J. Roy. Meteor. Soc.,* **124,** 2291–2297.

Huang, H.-P., and P. Sardeshmukh, 2000: Another look at the annual and semiannual cycles of atmospheric angular momentum. *J. Climate,* **13,** 3221–3228.

——, ——, and K. Weickmann, 1999: The balance of global and angular momentum in a long-term data set. *J. Geophys. Res.,* **104**, 2031–2040.

Juckes, M., I. James, and M. Blackburn, 1994: The influence of Antarctica on the momentum budget of the southern extratropics. *Quart. J. Roy. Meteor. Soc.,* **120,** 1017–1044.

Kang, I.-S., and K.-M. Lau, 1994: Principal modes of atmospheric circulation anomalies associated with global angular momentum fluctuations. *J. Atmos. Sci.,* **51,** 1194–1205.

Madden, R., and P. Speth, 1995: Estimates of atmospheric angular momentum, friction, and mountain torques during 1987–1988. *J. Atmos. Sci.,* **52,** 3681–3694.

Oort, A., 1989: Angular momentum cycle in the atmosphere-ocean-solid earth system. *Bull. Amer. Meteor. Soc.,* **70,** 1231–1242.

——, and E. Rasmusson, 1971: Atmospheric circulation statistics. NOAA Professional Paper 5, U.S. Government Printing Office, Washington, DC, 323 pp.

——, and J. Peixoto, 1983: Global angular momentum and energy balance requirements from observations. *Advances in Geophysics,*Vol. 25, Academic Press, 355–490.

Peixoto, J., and A. Oort, 1992: *Physics of Climate*. American Institute of Physics, 520 pp.

Rosen, R., D. Salstein, A. Miller, and K. Arpe, 1987: Accuracy of atmospheric angular momentum estimates from operational analyses. *Mon. Wea. Rev.,* **115,** 1627–1639.

——, ——, and T. Wood, 1991: Zonal contributions to global momentum variations on intraseasonal through interannual timescales. *J. Geophys. Res.,* **96,** 5145–5151.